LETTER

https://doi.org/10.1038/s41586-019-1463-1

Imaging magnetic polarons in the doped Fermi–Hubbard model

Joannis Koepsell[1]*, Jayadev Vijayan[1], Pimonpan Sompet[1], Fabian Grusdt[2,3], Timon A. Hilker[1,5], Eugene Demler[2], Guillaume Salomon[1], Immanuel Bloch[1,4] & Christian Gross[1]

Polarons—electronic charge carriers 'dressed' by a local polarization of the background environment—are among the most fundamental quasiparticles in interacting many-body systems, and emerge even at the level of a single dopant[1]. In the context of the two-dimensional Fermi–Hubbard model, polarons are predicted to form around charged dopants in an antiferromagnetic background in the low-doping regime, close to the Mott insulating state[2–7]; this prediction is supported by macroscopic transport and spectroscopy measurements in materials related to high-temperature superconductivity[8]. Nonetheless, a direct experimental observation of the internal structure of magnetic polarons is lacking. Here we report the microscopic real-space characterization of magnetic polarons in a doped Fermi–Hubbard system, enabled by the single-site spin and density resolution of our ultracold-atom quantum simulator. We reveal the dressing of doublons by a local reduction—and even sign reversal—of magnetic correlations, which originates from the competition between kinetic and magnetic energy in the system. The experimentally observed polaron signatures are found to be consistent with an effective string model at finite temperature[7]. We demonstrate that delocalization of the doublon is a necessary condition for polaron formation, by comparing this setting with a scenario in which a doublon is pinned to a lattice site. Our work could facilitate the study of interactions between polarons, which may lead to collective behaviour, such as stripe formation, as well as the microscopic exploration of the fate of polarons in the pseudogap and 'bad metal' phases.

Polarons usually occur in materials with a strong coupling between mobile charge carriers and collective modes of the background, such as phonons, magnons or spinons[1]. Furthermore, these materials often possess exotic properties, such as spin currents (in organic semiconductors)[9], colossal magnetoresistance (in manganites)[10], pseudogaps (in transition-metal oxides) or high-transition-temperature (high-T_c) superconductivity (in copper oxides)[11]. Even though there are many open questions regarding the microscopic description of these phenomena, some of them can be attributed to polarons, whereas others can emerge from multiple interacting polarons[1,12,13]. The most prominent and conceptually simple electronic model for high-T_c copper oxides is the two-dimensional doped Fermi–Hubbard model, in which an interplay between the kinetic energy of doped charge carriers and a magnetic background supports the formation of magnetic polarons at the single-dopant level. The model consists of spin-1/2 fermions hopping on a two-dimensional lattice with nearest-neighbour (NN) hopping amplitude t and on-site repulsion U between opposite spins. At half-filling, the ground state is a Mott insulating state with antiferromagnetic correlations, owing to an effective superexchange spin coupling of $J = 4t^2/U$. Upon hole or particle doping, dopants can lower their kinetic energy by delocalization. However, each hopping process of the dopant alters the spins of the magnetic background (see Fig. 1), which leads to a growing magnetic cost with increasing delocalization. This problem of a single dopant in an antiferromagnetic environment cannot be solved analytically and requires considerable effort to simulate its properties numerically. However, its understanding marks an important starting point for unravelling the physics of the doped Fermi–Hubbard model.

As a consequence of the competition between magnetic and kinetic energy, theoretical calculations of single dopants in the related t–J model predict the formation of a magnetic polaron[2–7], in which the dopant surrounds itself with a local cloud of reduced antiferromagnetic correlations (see Fig. 1a). Spectroscopic measurements of undoped copper oxides have experimentally probed this single-dopant regime. Even though measurements of dispersion or quasiparticle weights are compatible with the formation of polarons[8], a direct microscopic real-space image of such dressed charge carriers at the single-particle level is still lacking. Furthermore, the evolution from individual polarons into the pseudogap or the 'strange metal' phase at higher doping concentrations is still subject to controversy, leading to diverse theoretical approaches[11,14–16].

Quantum gas microscopy has enabled the direct, model-free real-space characterization of strongly correlated quantum many-body systems. In cold-atom lattice simulators[17], this technique has proved its potential to shed light on the Fermi–Hubbard model, including the detection of long-range spin correlations[18], charge and spin transport[19,20] in two dimensions, as well as incommensurate magnetism[21] in one dimension. Employing the full spin and density resolution of our setup[22], we experimentally confirm the presence and internal structure of magnetic polarons in the low-doping regime of a Fermi–Hubbard system. We observe how double occupations (doublons) are surrounded by a local distortion of antiferromagnetic correlations. Similar qualitative features of the spin correlations around the doublon, as measured in the experiment, are predicted by exact diagonalization of the t–J model, as well as an effective theory that models the polaron as a doublon bound to a spinon by a string of reduced antiferromagnetic correlations[7]. By contrast, by confining a doublon to a single lattice site with an optical tweezer, we observe qualitatively different signatures, underlining the necessity of delocalization for polaron formation.

In our experiment we prepared a balanced mixture of the two lowest hyperfine states of ^{6}Li and adiabatically loaded around 70 atoms into an anisotropic two-dimensional square lattice with spacings $(a_x, a_y) = (1.15, 2.3)\,\mu$m and depths $(8.6E_r^x, 3E_r^y)$, where $E_r^i = h^2/8ma_i^2$ is the recoil energy of the respective lattice, m is the atomic mass and h is the Planck constant. The system is well described by the two-dimensional Fermi–Hubbard model with approximately equal tunnelling amplitudes t_i in both directions, $t_y/h \approx t_x/h = 170$ Hz (see Methods). We tuned the interaction U by using the broad Feshbach resonance in ^{6}Li, such that $U/t_i = 14(1)$, leading to a superexchange coupling of $J/h = 50(5)$ Hz. All uncertainties reported here denote one standard deviation of the mean. We estimate the temperature T of the system to be $k_BT/t = 0.45^{+3}_{-1}$, where k_B is the Boltzmann constant (see Methods). In our study, we used doublon instead of hole doping, because doublons are trapped by our confining potential, avoiding contamination of the

[1]Max-Planck-Institut für Quantenoptik, Garching, Germany. [2]Department of Physics, Harvard University, Cambridge, MA, USA. [3]Department of Physics, Technical University of Munich, Garching, Germany. [4]Fakultät für Physik, Ludwig-Maximilians-Universität, Munich, Germany. [5]Present address: Cavendish Laboratory, University of Cambridge, Cambridge, UK.
*e-mail: joannis.koepsell@mpq.mpg.de

signal by holes created during the detection. A shown in Fig. 1, we realized separate settings in which doublons were allowed to hop between sites (Fig. 1a, left) or were pinned to a single lattice site (Fig. 1a, right). Mobile doublons were prepared using an increased chemical potential, resulting in delocalized doublons in the centre of our harmonically confined lattice with a trapping frequency of about $\omega/(2\pi) = 250$ Hz. For the preparation of immobile doublons we used a tightly focused laser beam (tweezer) at 702 nm with a waist of about 0.5 μm to form a deep attractive local potential. By shining the tweezer with appropriate intensity onto a single lattice site, the deep potential leads to an artificially created trapped doublon at that site (see Fig. 1a). Our detection method[22] allows us to simultaneously reconstruct the local spin and density within a single snapshot (see Fig. 1d). In this way, we can separate the spin and density sectors by measuring local spin correlations between two sites at positions $\boldsymbol{r}_1$ and $\boldsymbol{r}_2$ that are singly occupied (indicated by the filled circles below).

$$C(\boldsymbol{r}_1, \boldsymbol{r}_2) = 4\langle S^z_{\boldsymbol{r}_1} S^z_{\boldsymbol{r}_2}\rangle_{\bullet\boldsymbol{r}_1\bullet\boldsymbol{r}_2} \quad (1)$$

We define the value of $C(\boldsymbol{r}_1, \boldsymbol{r}_2)$ as the bond strength between $\boldsymbol{r}_1$ and $\boldsymbol{r}_2$. The spin environment around doublons can be investigated with a three-point doublon–spin correlator, which measures the two-point spin correlation as a function of a detected doublon (indicated by two filled circles) at a third position, $\boldsymbol{r}_0$

$$\begin{aligned} C(\boldsymbol{r}_0;\boldsymbol{r}_1,\boldsymbol{r}_2) &= 4\langle S^z_{\boldsymbol{r}_1} S^z_{\boldsymbol{r}_2}\rangle_{\vdots\boldsymbol{r}_0\bullet\boldsymbol{r}_1\bullet\boldsymbol{r}_2} \equiv C(\boldsymbol{r}_0;\boldsymbol{r},\boldsymbol{d}) \\ &= 4\left\langle S^z_{\boldsymbol{r}_0+\boldsymbol{r}-\frac{\boldsymbol{d}}{2}} S^z_{\boldsymbol{r}_0+\boldsymbol{r}+\frac{\boldsymbol{d}}{2}}\right\rangle_{\vdots\boldsymbol{r}_0\bullet\boldsymbol{r}_0+\boldsymbol{r}-\frac{\boldsymbol{d}}{2}\bullet\boldsymbol{r}_0+\boldsymbol{r}+\frac{\boldsymbol{d}}{2}} \end{aligned} \quad (2)$$

Here, the correlator is expressed in terms of the bond length $\boldsymbol{d} = \boldsymbol{r}_2 - \boldsymbol{r}_1$ of the spin correlation and the bond distance $\boldsymbol{r} = [(\boldsymbol{r}_1 + \boldsymbol{r}_2)/2] - \boldsymbol{r}_0$ from the doublon. This three-point correlator can be understood as defining the origin in each snapshot as the position of a detected doublon and calculating arbitrary two-point spin correlations as a function of distance from that point. For a magnetic polaron, this correlator is expected to reveal the strongly altered spin correlations in the immediate vicinity of doublons (that is, for small bond distances $\boldsymbol{r}$). The remainder of this article will focus on the analysis of $C(\boldsymbol{r}_0; \boldsymbol{r}, \boldsymbol{d})$ for NN ($|\boldsymbol{d}| = 1$), diagonal ($|\boldsymbol{d}| = 1.4$) and next-nearest-neighbour (NNN; $|\boldsymbol{d}| = 2$) spin correlations as a function of bond distance $\boldsymbol{r}$ from the doublons. Even in the Mott insulating regime without doping, quantum fluctuations of doublon–hole pairs lead to a constant background of detected doublons. To distinguish between doped particles and such naturally occurring fluctuations in our signal, we neglect double occupations with holes as NNs (see Methods).

Our access to three-point correlations allows us to study the local distortion of magnetic correlations surrounding doublons and therefore the inner structure of a polaron. Spins located close to a mobile doublon will be affected the strongest by doublon delocalization. Hence, the largest signal is expected for correlations between the four spins that are direct neighbours of a detected doublon; those are diagonal and NNN correlations. The NN correlations closest to the doublon, by contrast, exhibit a larger bond distance and are less sensitive to polaronic spin distortion. Therefore, we first consider the effect of doping on diagonal spin correlations and analyse the correlator defined in equation (2) to evaluate spin correlations as a function of bond distance $\boldsymbol{r}$ from doublons.

To study the doped system, we set the chemical potential such that a doped region of 5 × 3 sites forms with 1.95(1) doublons per experimental realization on average (see Fig. 2a). For each experimental snapshot, doublons are detected at different positions $\boldsymbol{r}_0$. We average the correlator of equation (2) over all positions in the doped region and obtain the average spin correlation around a single doublon $C(\boldsymbol{r}, \boldsymbol{d})$, as displayed in Fig. 2b for diagonal correlations ($|\boldsymbol{d}| = 1.4$). Remarkably, we observe the dressing of doublons with a spin disturbance, which

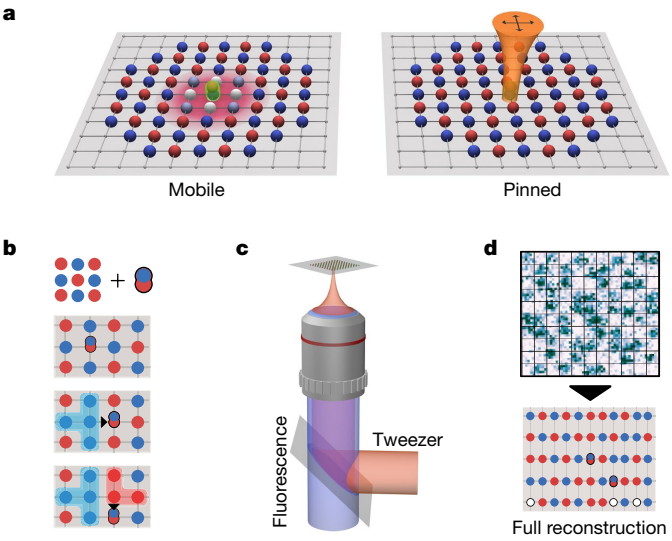

Fig. 1 | Mobile and immobile dopants with ultracold atoms. a, We experimentally study two-dimensional Fermi–Hubbard systems containing fermionic spin-up and spin-down particles (red and blue spheres, respectively), with mobile (left) or immobile (right) doublons (green), using a quantum gas microscope. In the mobile case, antiferromagnetic correlations close to the doublon are diminished (pink shading). This effect is absent in the immobile case, when the doublon is pinned with a focused attractive laser beam (orange). **b**, The hopping of a doublon (black arrow) in the antiferromagnetic background of the Fermi–Hubbard model around half-filling leads to a distorted spin order. With increasing delocalization, antiferromagnetically aligned spin pairs are turned into ferromagnetic ones (red and blue shading, highlighting ferromagnetic regions of different magnetization). As a consequence of this competition, theoretical and experimental evidence points towards polaron formation (see text). **c**, To create immobile localized doublons, we focus an attractive laser beam (orange) onto a single lattice site through the microscope, which collimates the fluorescence light (blue) for detection. **d**, Each captured image corresponds to a projected many-body quantum state. By employing our local Stern–Gerlach technique, we fully resolve spin and density (including holes, represented by white circles), enabling local investigation of the spin environment around doublons. As indicated in the reconstruced image, the Fermi–Hubbard model is implemented with equal tunnelling amplitudes, $t_y = t_x$, but unequal lattice spacings, $a_y = 2a_x$, to allow spin-resolved detection.

confirms the picture of a magnetic polaron. The strong effect on the magnetic correlations is even more pronounced in NNN correlations ($|\boldsymbol{d}| = 2$) across doublons, which reverse their sign with an amplitude a factor of two larger than that of diagonal correlations (see Fig. 2c). Numerical studies at low temperature have found that NNN spin correlations across dopants reverse their sign and become negative[23,24], which has been interpreted as local spin–charge separation and a building block of incommensurate magnetism in two dimensions[24,25]. Our results show that this effect persists even at elevated temperatures. In a frozen-spin picture, this sign reversal can be understood from a single displacement of the doublon (see Fig. 1b), which turns NN spins into NNN ones and thus automatically mixes a strong negative NN signal into the otherwise positive, but weaker, NNN correlations. A similar reasoning also applies to the sign reversal of diagonal spin correlations. Because antiferromagnetic NN correlations are stronger than any other spin correlation even at zero temperature, the string model intuitively predicts this sign flip to be robust also at lower temperatures. For a high enough density of dopants, even local two-point diagonal spin correlations (see equation (1)) can reverse their sign, as shown in Methods and reported in refs [26–28].

In addition, we analysed the correlations between doublons. At our temperature they appear anti-correlated at short distances and uncorrelated otherwise within our measurement uncertainty (see Methods). This is in agreement with other recent observations[28]

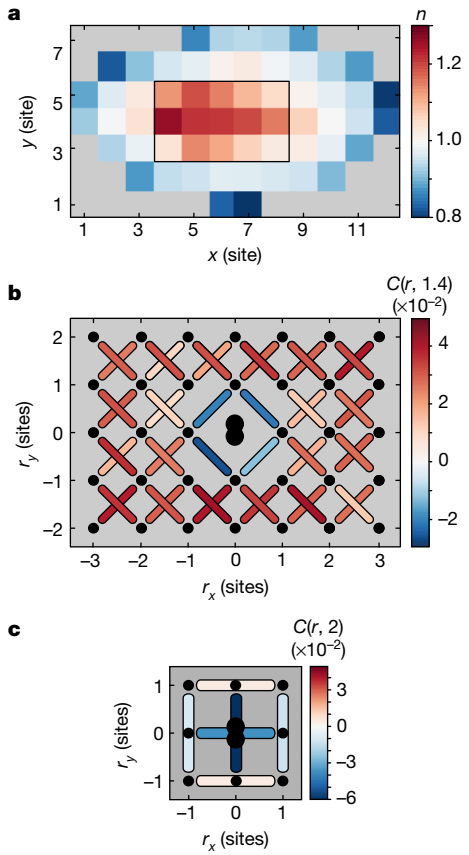

Fig. 2 | Mobile doublons dressed by local spin disturbance. a, Density (n) distribution for mobile doublons. In the doped region (inner black box), two doublons on average delocalize in an area of 5 × 3 sites. **b**, Diagonal spin correlations, represented by bonds connecting two sites (black dots) and sorted according to their distance from doublons (double black circle at centre). Correlations are negative only in the immediate vicinity of a doublon and positive farther away. **c**, NNN spin correlations across and next to detected doublons. As in the case of diagonal correlations (**b**),the correlations across doublons are sign-flipped with respect to the antiferromagnetic background value. Our experimental results confirm the formation of a magnetic polaron, in which doublons are dressed by a local spin distortion (see Fig. 1a, left).

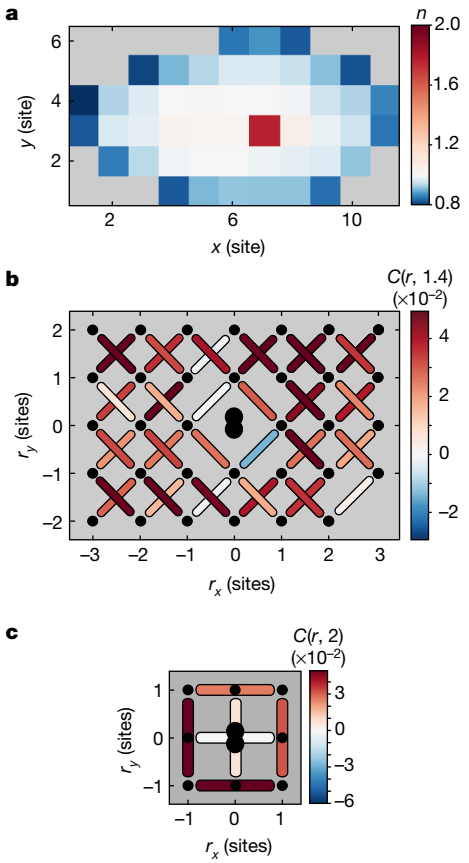

Fig. 3 | Spin correlations around trapped doublons. a, Density distribution for pinned doublons. An attractive laser beam (tweezer; 702 nm) focused on a single site artificially increases the density in an undoped system at a specific site to about 1.77(1). **b**, Diagonal spin correlations around doublons trapped in the tweezer. The sign-flipped spin distortion vanishes, in contrast to the mobile case. **c**, NNN spin correlations across and next to pinned doublons. Although spins across the trapped doublon are uncorrelated, correlations neighbouring the trapped doublon are slightly enhanced compared to the background value (see Fig. 4c). Trapping doublons with a tweezer beam prevents the competition between kinetic and magnetic energy and suppresses polaron formation (see Fig. 1a, right).

and supports our treatment of each doublon as an independent fermionic particle.

To demonstrate that the mobility of the doublon is key for polaron formation, we now investigate the effect of an artificially introduced localized doublon on the surrounding magnetic correlations. We set the chemical potential so as to prepare a system without doping and we adiabatically ramp up the power of an optical tweezer focused on a single central site while simultaneously ramping up the lattice. The final tweezer depth is set such that the density of that site saturates at 1.77(1) (see Fig. 3a). We do not achieve a perfectly deterministic doublon preparation in our experiments, probably because of detection errors and higher-band effects (see Methods). We analyse the same doublon-conditioned three-point correlator $C(\boldsymbol{r}_0; \boldsymbol{r}, \boldsymbol{d})$ for diagonal spin correlations, as before, with $\boldsymbol{r}_0$ fixed to the pinned site (see Fig. 3b). As expected, the strong spin distortion and, most importantly, the sign reversal of correlations is absent in this case. Instead, magnetic correlations across the trapped site are only moderately reduced compared to the undoped background (see Fig. 3c).

To enable a quantitative study and a comparison to theoretical models, we group the three-point spin correlations by the magnitude of their bond distance $r = |\boldsymbol{r}|$ from doublons. Measured NN, diagonal and NNN spin correlations are shown in Fig. 4. The local distortion of spin correlations around mobile doublons is visible in all correlators. Sign reversal of diagonal and NNN correlations occurs at a mean bond distance of one site, yielding a diameter (and estimated polaron size) of around two lattice sites. We compare our findings to theoretical model calculations carried out for the estimated temperature of our system (see Fig. 4). For the mobile case, an effective string model of magnetic polarons is used, assuming frozen spin dynamics[7]. Remarkably, similar amplitude changes of correlations, and hence a similar polaron radius, is predicted (also found in the exact diagonalization results of the t–J model on a 4 × 4 system; see Supplementary Information). Furthermore, the sign changes of correlations in the vicinity of the doublon are reproduced in this model, as seen also in Fig. 4e, f. Quantitative differences between the effective model and the experiment remain; however, this is expected owing to the moderate separation of spin and hole dynamics ($J/t = 0.3$) and the elevated temperatures in the experimental system. In the case of pinned doublons, two effects can be observed. First, the sign flip of correlations observed in the mobile case vanishes and the closest-distance diagonal and NNN spins appear uncorrelated; this is captured by an exact diagonalization calculation of the t–J model with zero tunnelling of the excess doublon (see Fig. 4). This can be explained by the fact that the doublon effectively blocks a path linking the spins next to it and prevents them from building up a correlation, given the finite temperature. Second, an enhancement of certain spin correlations around the pinned site is visible in the closest NN correlations and distance-1 NNN correlations. This effect is expected from

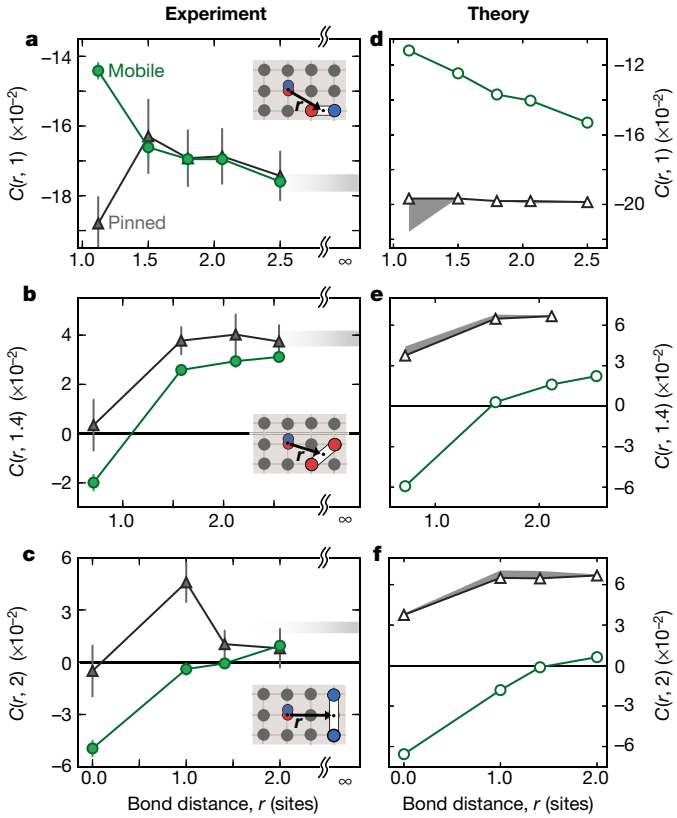

Fig. 4 | Spin correlations as a function of bond distance from doublons. **a**–**f**, Comparison between experiment (**a**–**c**) and numerical calculations performed using a string model for magnetic polarons and exact diagonalization of an immobile doublon in the *t*–*J* model (**d**–**f**). NN (**a**, **d**), diagonal (**b**, **e**) and NNN (**c**, **f**) spin correlations as a function of bond distance from mobile (green) or immobile (black) doublons. The insets show one examplary bond (white) between two particles and its distance ***r*** from a doublon (double circle). Error bars denote one standard error of the mean (s.e.m.). For mobile doublons, diagonal and NNN correlations within an average bond distance of one lattice site are sign-flipped with respect to the antiferromagnetic background. Correlations quickly recover at larger distances to a value approaching the undoped antiferromagnetic value, represented by the grey band at distance ∞ with a width of 2 s.e.m. The string model (green in **d**–**f**) predicts similar correlation changes with bond distance, as well as the sign reversal of diagonal and NNN correlations. For pinned doublons, the diagonal and NNN correlations at the smallest bond distance are not sign-flipped and the polaronic distortion is strongly reduced. The amplitude of the remaining weakening of the magnetic correlations is consistent with exact diagonalization calculations of a trapped doublon (black in **d**–**f**). Owing to the finite tweezer size (see text), a slight enhancement of NN and NNN correlations around a distance of one site is visible in the experiment, which can be captured by exact diagonalization with 10% enhanced spin exchange on neighbouring sites (grey band).

local energy shifts around the pinned site that are caused by the finite extent of the optical-tweezer beam (see Methods). Those energy shifts lead to a locally enhanced superexchange coupling *J* and can therefore cause stronger correlations. Exact diagonalization calculations at finite temperature with up to 10% increased superexchange coupling in the vicinity reproduce our experimental correlation enhancement (see Methods). Nonetheless, correlations across the doublon and the shortest-distance diagonal correlations are almost unaffected by this small systematic enhancement.

We have presented single-particle-resolution imaging of a magnetic polaron in a doped Fermi–Hubbard system by revealing the dressing of mobile doublons with a spin distortion. We identified a compact polaron size of about two sites and characterized its inner structure, in which spin correlations can exhibit even sign reversal compared to the undoped system. Our findings qualitatively agree with numerical predictions. Artificially localizing the doublon considerably reduces the spin distortion and the sign flip disappears, as the competition between kinetic and magnetic energy is suppressed. The ability to spatially resolve the dressing cloud of polarons enables a fundamentally new approach to experimentally characterizing such quasiparticles at the microscopic level and could be applied to study the polaron physics of impurities immersed in bosonic[29] or fermionic gases[30] and provide observables for the exploration of strongly correlated phenomena and their microscopic origin. In the future, the effective mass or the quasiparticle weight of the polaron could be probed by transport[19,20] or spectroscopic methods[31]. By implementing larger and more homogeneous systems, as well as new cooling schemes[18,32,33], a microscopic study of polaron–polaron interactions and the crossover from polarons to the emergence of pseudogap, strange-metal and stripe phases or pairing is within reach.

Online content

Any methods, additional references, Nature Research reporting summaries, source data, extended data, supplementary information, acknowledgements, peer review information; details of author contributions and competing interests; and statements of data and code availability are available at https://doi.org/10.1038/s41586-019-1463-1.

Received: 16 November 2018; Accepted: 10 June 2019;
Published online 14 August 2019.

1. Alexandrov, S. & Devreese, J. T. *Advances in Polaron Physics* (Springer, 2010).
2. Schmitt-Rink, S., Varma, C. M. & Ruckenstein, A. E. Spectral function of holes in a quantum antiferromagnet. *Phys. Rev. Lett.* **60**, 2793–2796 (1988).
3. Shraiman, B. I. & Siggia, E. D. Mobile vacancies in a quantum Heisenberg antiferromagnet. *Phys. Rev. Lett.* **61**, 467–470 (1988).
4. Sachdev, S. Hole motion in a quantum Néel state. *Phys. Rev. B* **39**, 12232–12247 (1989).
5. Kane, C. L., Lee, P. A. & Read, N. Motion of a single hole in a quantum antiferromagnet. *Phys. Rev. B* **39**, 6880–6897 (1989).
6. Dagotto, E., Moreo, A. & Barnes, T. Hubbard model with one hole: ground-state properties. *Phys. Rev. B* **40**, 6721–6725 (1989).
7. Grusdt, F. et al. Parton theory of magnetic polarons: mesonic resonances and signatures in dynamics. *Phys. Rev. X* **8**, 011046 (2018).
8. Schrieffer, J. R. *Handbook of High-Temperature Superconductivity* (Springer, 2007).
9. Watanabe, S. et al. Polaron spin current transport in organic semiconductors. *Nat. Phys.* **10**, 308–313 (2014).
10. Ramirez, A. P. Colossal magnetoresistance. *J. Phys. Condens. Matter* **9**, 8171–8199 (1997).
11. Lee, P. A., Nagaosa, N. & Wen, X.-G. Doping a Mott insulator: physics of high-temperature superconductivity. *Rev. Mod. Phys.* **78**, 17–85 (2006).
12. Trugman, S. A. Interaction of holes in a Hubbard antiferromagnet and high-temperature superconductivity. *Phys. Rev. B* **37**, 1597–1603 (1988).
13. Schrieffer, J. R., Wen, X. & Zhang, S. C. Dynamic spin fluctuations and the bag mechanism of high-T_c superconductivity. *Phys. Rev. B* **39**, 11663–11679 (1989).
14. Anderson, P. W. The resonating valence bond state in La_2CuO_4 and superconductivity. *Science* **235**, 1196–1198 (1987).
15. Auerbach, A. & Larson, B. E. Small-polaron theory of doped antiferromagnets. *Phys. Rev. Lett.* **66**, 2262–2265 (1991).
16. Punk, M., Allais, A. & Sachdev, S. Quantum dimer model for the pseudogap metal. *Proc. Natl Acad. Sci. USA* **112**, 9552–9557 (2015).
17. Gross, C. & Bloch, I. Quantum simulations with ultracold atoms in optical lattices. *Science* **357**, 995–1001 (2017).
18. Mazurenko, A. et al. A cold-atom Fermi–Hubbard antiferromagnet. *Nature* **545**, 462–466 (2017).
19. Brown, P. T. et al. Bad metallic transport in a cold atom Fermi–Hubbard system. *Science* **363**, 379–382 (2019).
20. Nichols, M. A. et al. Spin transport in a Mott insulator of ultracold fermions. *Science* **363**, 383–387 (2019).
21. Salomon, G. et al. Direct observation of incommensurate magnetism in Hubbard chains. *Nature* **565**, 56–60 (2019); correction 566, E5 (2019).
22. Boll, M. et al. Spin- and density-resolved microscopy of antiferromagnetic correlations in Fermi–Hubbard chains. *Science* **353**, 1257–1260 (2016).
23. White, S. R. & Scalapino, D. Hole and pair structures in the t–J model. *Phys. Rev. B* **55**, 6504–6517 (1997).
24. Martins, G. B., Eder, R. & Dagotto, E. Indications of spin-charge separation in the two-dimensional t–J model. *Phys. Rev. B* **73**, 170–173 (1999).
25. Martins, G. B., Gazza, C., Xavier, J. C., Feiguin, A. & Dagotto, E. Doped stripes in models for the cuprates emerging from the one-hole properties of the insulator. *Phys. Rev. Lett.* **84**, 5844–5847 (2000).
26. Parsons, M. F. et al. Site-resolved measurement of the spin-correlation function in the Fermi–Hubbard model. *Science* **353**, 1253–1256 (2016).

27. Cheuk, L. W. et al. Observation of spatial charge and spin correlations in the 2D Fermi–Hubbard model. *Science* **353**, 1260–1264 (2016).
28. Chiu, C. S. et al. String patterns in the doped Hubbard model. Preprint at https://arxiv.org/abs/1810.03584 (2018).
29. Devreese, J. T. & Alexandrov, A. S. Froehlich polaron and bipolaron: recent developments. *Rep. Prog. Phys.* **72**, 066501 (2009).
30. Radzihovsky, L. & Sheehy, D. E. Imbalanced Feshbach-resonant Fermi gases. *Rep. Prog. Phys.* **73**, 076501 (2010).
31. Stewart, J. T., Gaebler, J. P. & Jin, D. S. Using photoemission spectroscopy to probe a strongly interacting Fermi gas. *Nature* **454**, 744–747 (2008).
32. Lubasch, M., Murg, V., Schneider, U., Cirac, J. I. & Bañuls, M.-C. Adiabatic preparation of a Heisenberg antiferromagnet using an optical superlattice. *Phys. Rev. Lett.* **107**, 165301 (2011).
33. Kantian, A., Langer, S. & Daley, A. J. Dynamical disentangling and cooling of atoms in bilayer optical lattices. *Phys. Rev. Lett.* **120**, 060401 (2018).

METHODS

Experimental sequence. The preparation of cold Fermi–Hubbard systems closely followed the procedure described in Salomon et al.[21]. We started by preparing a balanced mixture of the two lowest hyperfine states of fermionic ^{6}Li (hyperfine and magnetic quantum numbers of $F = 1/2$ and $m_F = \pm 1/2$), which was harmonically confined in a single two-dimensional plane of a $40E_r^z$-deep optical lattice with 3.1 μm spacing in the z direction. The final atom number was set by the evaporation parameters. Subsequently, we ramped the depth of the x and y lattices with spacings of $a_x = 1.15$ μm and $a_y = 2.3$ μm linearly from $0E_r^i$ to their final values of $8.6E_r^x$ and $3E_r^y$ within 210 ms. The final lattice depths were optimized with undoped Mott insulators to give strong and isotropic spin correlations. From band-width calculations we extracted the tight-binding NN tunnelling amplitudes $t_x/h = 170$ Hz and $t_y/h = 180$ Hz. The NNN tunnelling amplitude along the y direction was below $0.1t_y$. Using the broad Feshbach resonance of ^{6}Li, the scattering length was tuned during the lattice ramp from $350a_B$ to $2150a_B$ in two linear ramps, where a_B denotes the Bohr radius. The first one ramped to $980a_B$ within 150 ms and the second ramp increased the scattering length to $2150a_B$ in 60 ms. By applying a local Stern–Gerlach detection technique[22] and subsequent Raman sideband cooling in a pinning lattice[34], the local spin and density of each lattice site was obtained with an average fidelity of 97%.

Data analysis. The work presented here used a dataset for pinned doublons and one for mobile doublons consisting of 33,669 and 9,002 images, respectively. In the analysis, we considered only shots with total spin $|S^z_{tot}| \leq 3.5$, in order to filter out fluctuations in our spin detection scheme[21] and strongly magnetized clouds. This corresponds to a maximum allowed magnetization of $|S^z_{tot}|/N \approx 0.05$ and approximately 68% of the images recorded. All further analysis was performed on lattice sites with a mean density of $n \geq 0.7$. This region corresponds to the sites shown in Figs. 2a, 3a for the mobile and pinned cases, respectively. To exclude clouds heated from inelastic three-body collisions, images with a total number of holes of $\sum_{ROI} n_h \geq 8$ contained in this region of interest were discarded (which amounts to neglecting around 16% of the data). Computing the doublon–hole correlation function $g_2 = [\langle \hat{n}_d \hat{n}_h \rangle / (\langle \hat{n}_d \rangle \langle \hat{n}_h \rangle)] - 1$ reveals doublon–hole bunching at NN distances (see Extended Data Fig. 1), which indicates the presence of doublon–hole fluctuations. To distinguish between doped excess doublons and doublon–hole fluctuations, we excluded doublons with holes as NNs from the analysis. The resulting dataset statistics after processing is shown in Extended Data Fig. 2 for the mobile case.

Doping calibration. To control the doping, we measured the number of double occupations per number of atoms (N_{doub}/N) in our system as a function of the mean atom number N (see Extended Data Fig. 3a), which is set by our final evaporation parameters. For low atom numbers, the doublon fraction saturates below 4%, which we attribute to quantum fluctuations in the form of doublon–hole pairs. The background of doublon–hole fluctuations is confirmed by discarding doublons with holes as NNs, obtaining the curve of doped doublons versus total atom number shown in Extended Data Fig. 3b. For low atom numbers, no doped doublons are present, whereas at higher atom numbers finite doping sets in. To probe individual mobile doublons in the Fermi–Hubbard model, we used systems with about 72 atoms and around two doped doublons. To study the effect of localized doublons created using an optical tweezer (see below), we used smaller systems with around 55 atoms to avoid the effect of doping.

Tweezer depth calibration. For the pinned doublon case, we ramped the power of an optical tweezer beam focused on a single lattice site to its final value simultaneously with the x and y lattice depth. The tweezer depth was calibrated in a separate measurement by determining the density of the target site as a function of the final tweezer power. As shown in Extended Data Fig. 4, the density first increases with power and then saturates below 1.8, independent of higher final powers. The total detected local density n of 1.77 is $n = 3 \times n_t + 2 \times n_d + 1 \times n_s + 0 \times n_h$, where n_t, n_d, n_s and n_h are the triplon, doublon, singlon and hole density, respectively. For our measurement of localized doublons, we set the tweezer depth to the value at which the density starts saturating. At this tweezer power, the hole density at that site is $n_h = 0.07$, the singlon density is $n_s = 0.13$, the doublon density is $n_d = 0.74$ and a small triplon density of $n_t = 0.05$ exists, which we attribute to imperfections in the detection of doublons, imperfections in the loading procedure and coupling of the y direction to higher bands. In combination with our finite imaging fidelity of 97%, this explains why a deterministic preparation of the doublon is not fully achieved.

Tweezer effect on neighbouring sites. Considering our experimental point-spread function and our numerical aperture of 0.5, the intensity of the 702-nm light radially falls off to 30% at a distance of 600 nm from the maximum. Our point-spread function furthermore shows two asymmetric distorted side-maxima with around 10% intensity, and imperfections in our compensation of the chromatic focal shift between our imaging light at 671 nm and the tweezer beam at 702 nm will lead to a finite-energy shift on neighbouring sites. The total tweezer depth can be approximated by the interaction energy U, and we expect that neighbouring sites (especially in the x direction) are shifted in energy by up to $0.3U$. Such a detuning alters the spin exchange between those sites according to $J = 2t^2[1/(U + \Delta) + 1/(U - \Delta)]$ (ref. [35]). As mentioned in the main text, this explains the enhancement of certain spin correlations around the pinned site and is consistent with the slightly increased average densities on the left (right) of the pinned site in the x direction to 1.024(5) (1.059(5)). When modelling this effect in exact diagonalization calculations, an enhanced spin exchange of 10% between all eight sites surrounding the pinned doublon was assumed.

Temperature estimation. To estimate the temperature of the clouds, we compared the loss-corrected NN spin correlations $\langle S^z_r S^z_{r+e_i} \rangle$, where $e_i = \{e_x, e_y\}$, close to half-filling with numerical linked-cluster expansions up to ninth order for homogeneous systems[36]. We used Wynn's algorithm[37] to sum the terms of the series and obtain NN spin correlations as a function of the density for $U/t = 13$. This value is the lowest estimate of the interaction strength U and takes into account the renormalization for low lattice depths[38]. The experimental spin correlations as a function of density were obtained by averaging over sites with local densities between 0.9 and 1.1 in bins ranging from 0.02 to 0.04 to collect enough statistics. We find that our experimental correlations compare well with numerical linked-cluster expansion results at a temperature of $T \in [0.43t, 0.46t]$ (see Extended Data Fig. 5). To account for the uncertainty in the exact interaction U, we conservatively estimate our temperature to be $k_B T/t = 0.45^{+3}_{-1}$ (see Extended Data Fig. 5). Neither the experimental nor the numerical results have a substantial dependence on temperature with respect to such temperature changes.

Doublon–doublon correlations. Possible interactions between doped excess doublons can be detected by the normalized density–density g_2 correlation function $g_2(\boldsymbol{r}_1, \boldsymbol{r}_2) = [\langle \hat{n}_d(\boldsymbol{r}_1) \hat{n}_d(\boldsymbol{r}_2) \rangle / (\langle \hat{n}_d(\boldsymbol{r}_1) \rangle \langle \hat{n}_d(\boldsymbol{r}_2) \rangle)] - 1$. Here, the operator $\hat{n}_d$ measures the density of real excess doublons without doublon–hole fluctuations. As seen in Extended Data Fig. 6, doublons are anti-correlated at short distances and quickly become uncorrelated within our measurement precision. The anti-correlation is expected for free fermions and our current statistical uncertainty does not allow us to resolve possible small interaction effects at the realized temperature.

Extended polaron analysis. The spin correlator $C(\boldsymbol{r}, \boldsymbol{d})$ discussed in the main text was used to determine the polaronic spin environment of mobile doublons. This correlator is the result of averaging $C(\boldsymbol{r}_0; \boldsymbol{r}, \boldsymbol{d})$ over the positions $\boldsymbol{r}_0$ of mobile doublons. Here we show that the spin distortion is consistently dressing the doublon, independently of the position in the trap. We study the NN, diagonal and NNN correlations with the shortest bond distance $\boldsymbol{r}$ to the doublon as a function of position $\boldsymbol{r}_0$. To maintain a sufficiently high signal-to-noise ratio, we average bonds isotropically. Furthermore, we contrast this to the case in which the position $\boldsymbol{r}_0$ is singly occupied instead

$$C_{singlon}(\boldsymbol{r}_0; \boldsymbol{r}, \mathbf{d}) \equiv C_{singlon}(\boldsymbol{r}_0; \boldsymbol{r}_1, \boldsymbol{r}_2) = 4 \langle S^z_{r_1} S^z_{r_2} \rangle_{\bullet \boldsymbol{r}_0 \bullet \boldsymbol{r}_1 \bullet \boldsymbol{r}_2} \quad (3)$$

The total correlation strength for those two different cases is shown in Extended Data Fig. 7 as a function of position $\boldsymbol{r}_0$ in the system for NN, diagonal and NNN correlations. A strong difference in the local spin environment is observed, depending on whether a doublon or singlon is present at a specific site. The spin distortion that dresses the doublon is strongest for NNN correlations and weakest for NN correlations, which can be understood by considering that NNN correlations are much closer (bond distance 0) to the doublon than NN correlations (bond distance of 1.1). When a singlon occupies a certain position, the strong spin distortion is absent. In this case, the spin correlation surrounding the singlon does not fully return to the background value of an undoped system, because polarons are still present in the system and their average distance from the singlon is of the order of one to two lattice sites. This is also responsible for the varying correlation strength of singlons at different positions. When the singlon is considered in regions of higher density, the average distance to polarons decreases, leading to a parasitic reduction in correlation strength.

Diagonal two-point spin correlations. Two-point spin correlations along the lattice diagonal are shown in Extended Data Fig. 8. In regions with high doublon density (see lattice site positions in Fig. 2a), these two-point correlations flip their sign.

NN spin correlations. Two- and three-point NN spin correlations (equations (1), (2) with $|\boldsymbol{d}| = 1$) are shown in Extended Data Fig. 9. The spin distortion dressing mobile doublons is also visible here. Nonetheless, as explained above, the signal-to-noise ratio is weaker than for the other correlators. In Extended Data Fig. 9c, NN correlations are shown for the case of pinned doublons. The local enhancement of correlations is visible at the closest bond distance.

Data availability

The datasets generated and analysed during this study are available from the corresponding author upon reasonable request.

34. Omran, A. et al. Microscopic observation of Pauli blocking in degenerate fermionic lattice gases. *Phys. Rev. Lett.* **115**, 263001 (2015).

35. Trotzky, S. et al. Time-resolved observation and control of superexchange interactions with ultracold atoms in optical lattices. *Science* **319**, 295–299 (2008).
36. Khatami, E. & Rigol, M. Thermodynamics of strongly interacting fermions in two-dimensional optical lattices. *Phys. Rev. A* **84**, 053611 (2011).
37. Rigol, M., Bryant, T. & Singh, R. R. P. Numerical linked-cluster algorithms. I. Spin systems on square, triangular, and kagomé lattices. *Phys. Rev. E* **75**, 061118 (2007).
38. Büchler, H. P. Microscopic derivation of Hubbard parameters for cold atomic gases. *Phys. Rev. Lett.* **104**, 090402 (2010).

Acknowledgements We thank D. Stamper-Kurn, Y. Wang, E. Manousakis, S. Sachdev and T. Giamarchi for discussions. This work benefited from financial support by the Max Planck Society (MPG), the European Union (UQUAM, FET-Flag 817482, PASQUANS) and the Max Planck Harvard Research Center for Quantum Optics (MPHQ). J.K. gratefully acknowledges funding from Hector Fellow Academy. F.G. and E.D. acknowledge support from Harvard-MIT CUA, NSF grant number DMR-1308435 and AFOSR-MURI Quantum Phases of Matter (grant FA9550-14-1-0035). F.G. acknowledges financial support from the Gordon and Betty Moore Foundation through the EPiQS programme and from the Technical University of Munich – Institute for Advanced Study, funded by the German Excellence Initiative and the European Union FP7 under grant agreement 291763, from DFG grant number KN 1254/1-1 and DFG TRR80 (Project F8).

Author contributions J.K., J.V., P.S., T.A.H., G.S., I.B. and C.G. planned the experiment and analysed and discussed the data. F.G. and E.D. performed the theoretical simulations. All authors contributed to the interpretation of the data and writing of the manuscript.

Competing interests The authors declare no competing interests.

Additional information
Supplementary information is available for this paper at https://doi.org/10.1038/s41586-019-1463-1.
Correspondence and requests for materials should be addressed to J.K.

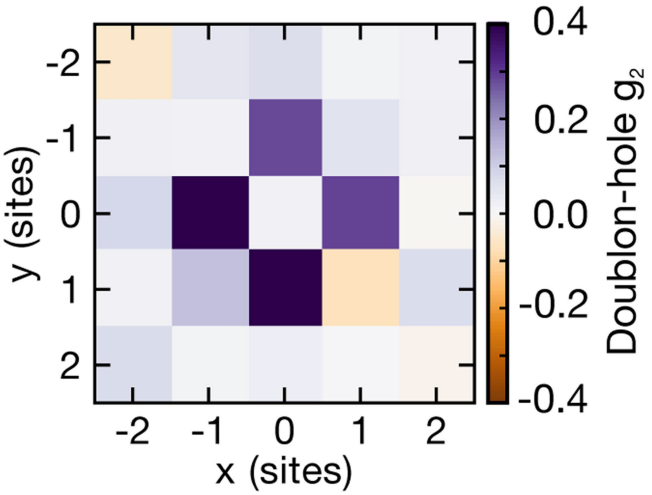

Extended Data Fig. 1 | Doublon–hole correlation. Two-point correlation function g_2 between double occupations and holes, showing a strong bunching effect at NN distances. This motivates us to neglect double occupations with holes as NNs in the analysis of mobile doublons.

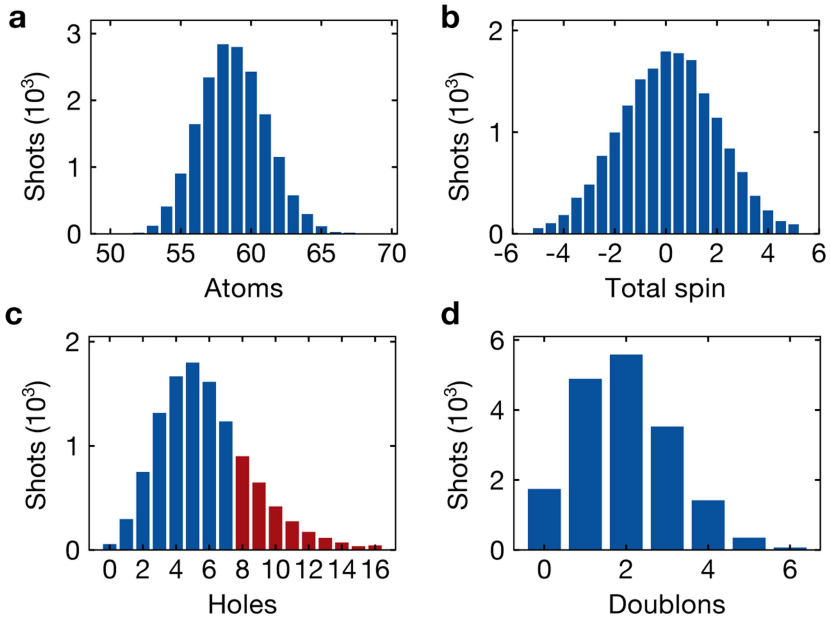

Extended Data Fig. 2 | Dataset statistics for the measurement of mobile doublons. a–c, Distribution of the number of atoms (**a**), spins (**b**) and holes (**c**) in the region with density greater than 0.7. Red bars in **c** indicate shots discarded by the applied hole filter (see text). **d**, Number of mobile doublons (doublon–hole fluctuations subtracted) in the doped 5 × 3-site region.

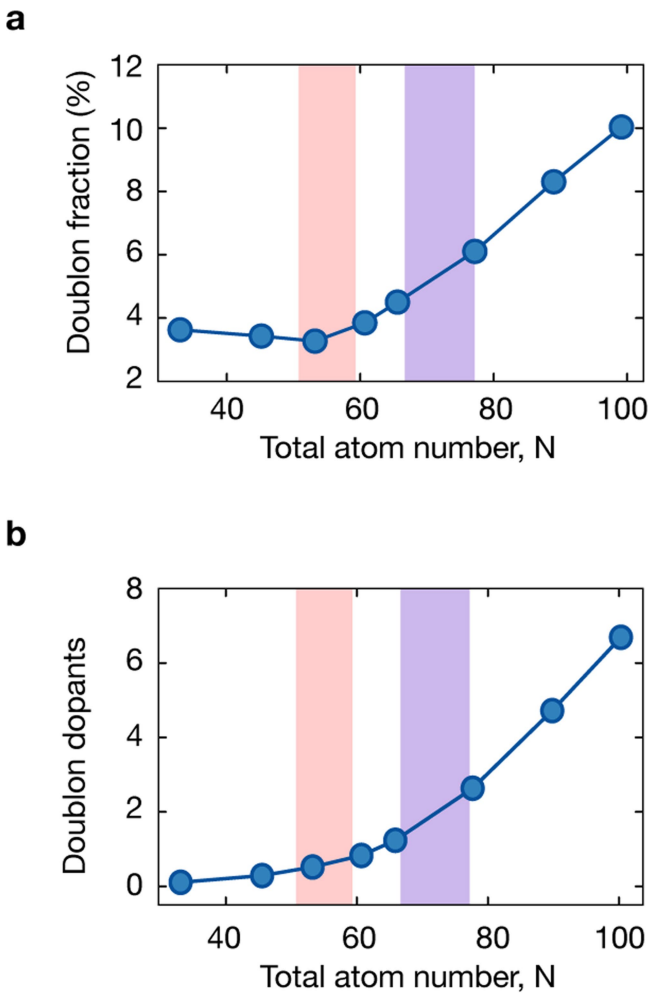

Extended Data Fig. 3 | Doping calibration. a, **b**, When scanning our final evaporation parameters, we measured the fraction of double occupations (**a**)and the number of doped doublons (**b**; excluding doublon–hole fluctuations) in the system as a function of the mean total atom number, *N*. Statistical error bars are smaller than the marker size. Pinned doublon measurements were taken in an undoped system (pink bar). For the mobile doublon dataset, settings for weak doping were used (purple bar). The bar width represents the standard deviation, obtained from atom number fluctuations.

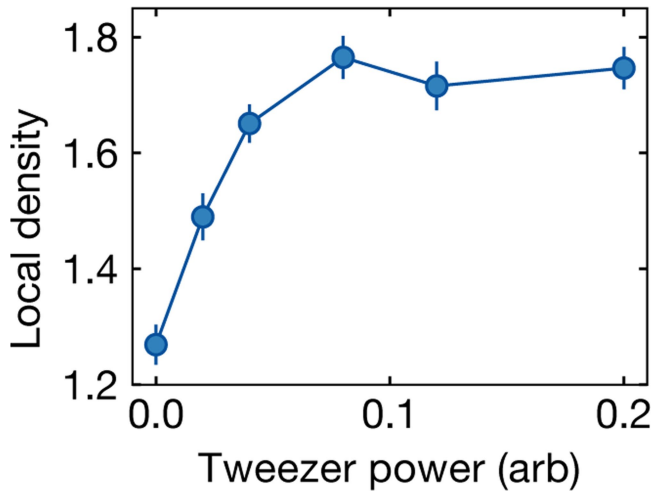

Extended Data Fig. 4 | Calibration of tweezer power. Density of the lattice site on which the tweezer is focused as a function of final tweezer power. Error bars denote one s.e.m. For the realization of pinned doublons the power was set to 0.11 (arbitrary units).

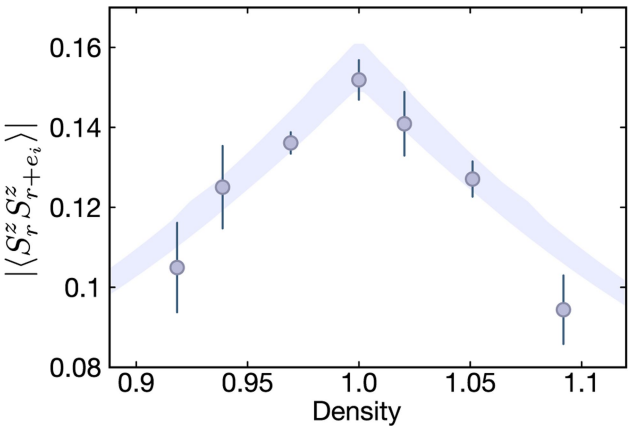

Extended Data Fig. 5 | Temperature estimation. Two-point NN spin correlations as a function of binned density. Error bars denote one s.e.m. Upper (lower) values of the purple band correspond to temperatures of $T/t = 0.43$ (0.46) in numerical linked-cluster expansions at $U/t = 13$.

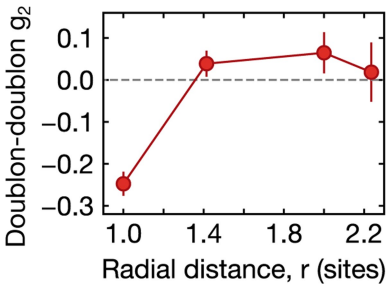

Extended Data Fig. 6 | Radially averaged doublon–doublon correlation function, g_2. In our system, excess doublons appear anti-correlated at short distances and quickly become uncorrelated at longer distances. Error bars denote one s.e.m.

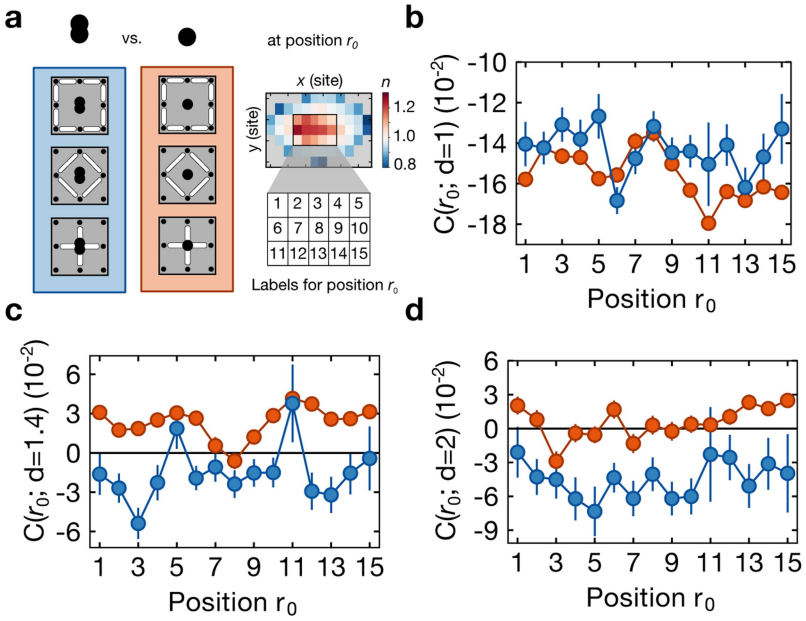

Extended Data Fig. 7 | Extended polaron analysis. a, Comparison of the local spin environment around a lattice site $\boldsymbol{r}_0$ occupied by a doublon (double black circle) or a singlon (single black circle). To simplify the notation, site positions in the doped region of our system are labelled from 0 to 15 (see inset at right). At any position in the 5 × 3-site system, spin distortion is present in NN (**b**), diagonal (**c**) and NNN (**d**) correlations whenever a doublon is detected (blue), and absent whenever a singlon is detected (red). Error bars denote one s.e.m. NNN correlations are measured across doublons and have a high signal-to-noise ratio, which we attribute to their short bond distance of 0, compared to, for example, NN correlations (bond distance of 1.1).

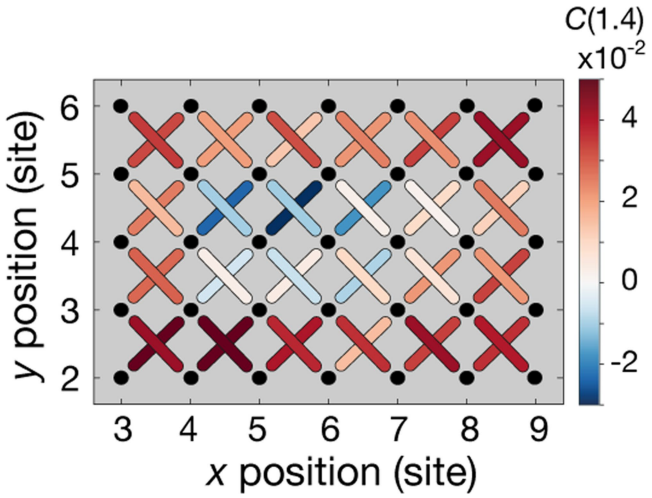

Extended Data Fig. 8 | Diagonal two-point spin correlations. Spin correlations in the central region (see lattice site positions in Fig. 2), represented by bonds connecting the two sites (black dots). At the centre, a clear reduction of correlations from the positive antiferromagnetic background value is visible. In the area of highest doublon density, correlations even flip sign and become negative.

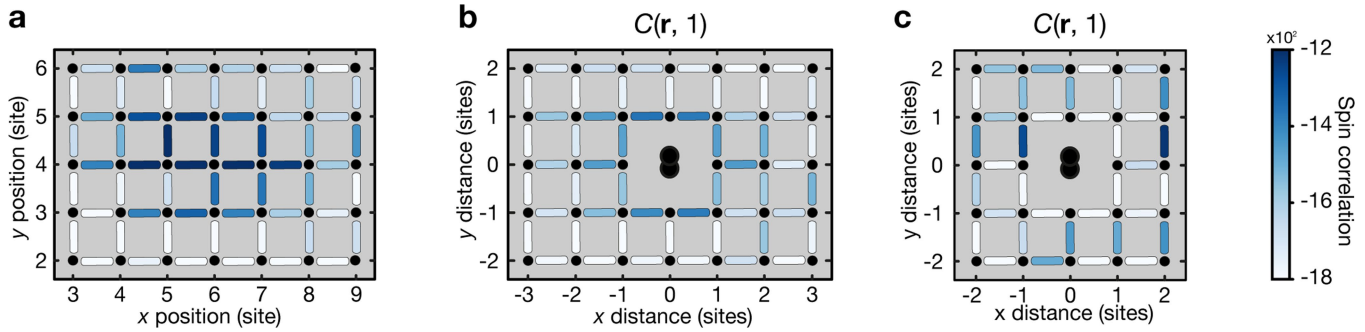

Extended Data Fig. 9 | NN correlations around mobile or pinned doublons. a, Two-point NN correlations in the central region for the mobile doublon setting, represented by colored bonds between lattice sites (black dots). **b**, NN spin correlations as a function of distance from mobile doublons. **c**, NN correlations around pinned doublons. The enhancement effect of correlations is visible in the strong bonds surrounding the trapping site.